

Compact Hadamard Latent Codes for Efficient Spectral Rendering

JIAQI YU, DAR'YA GUARNERA, and GIUSEPPE CLAUDIO GUARNERA, University of York, United Kingdom

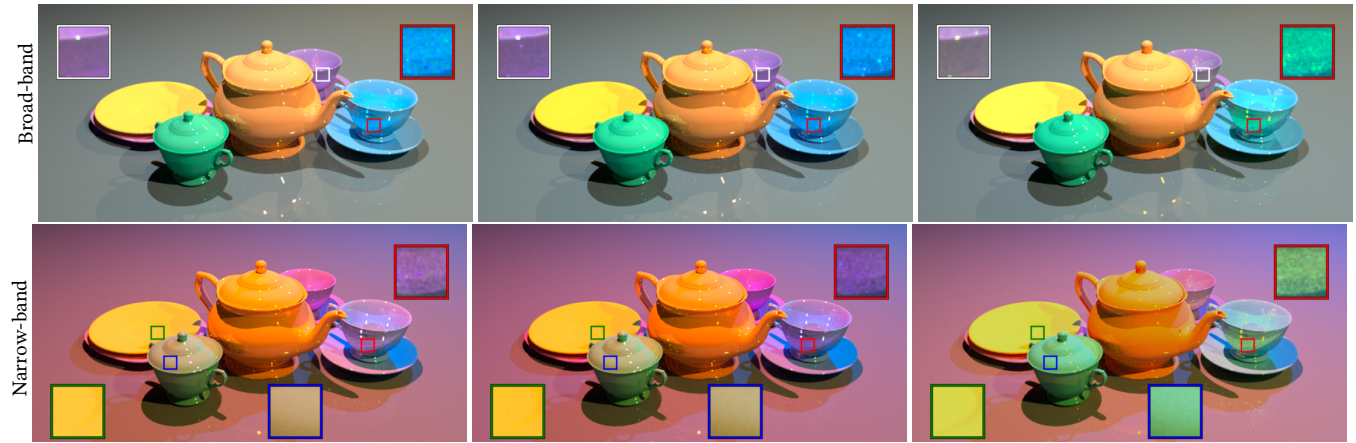


Fig. 1. Spectral rendering with compact Hadamard codes ($k = 6$, requiring only 2 RGB passes). **Top row**: broad-band illumination; **bottom row**: narrow-band illumination. Our method (a) achieves perceptually accurate results compared to full spectral rendering ground truth (b), while standard RGB rendering (c) exhibits significant color shifts, particularly under narrow-band illumination. Insets show zoomed regions highlighting material appearance differences.

Spectral rendering accurately reproduces wavelength-dependent appearance, but is expensive because each shading operation must be evaluated at dozens of wavelength samples and scales roughly linearly with the number of wavelength samples. Furthermore, it requires spectral textures and lights throughout the pipeline. We propose *Hadamard spectral codes*, a compact latent representation that enables spectral rendering and can be manipulated by the same operations used in standard RGB renderers, so that spectral rendering can be approximated using a small number of standard RGB rendering passes, followed by a decode step. Our key requirement is *latent linearity*: scaling and addition in spectral space map to scaling and addition of codes, and the element-wise product of spectra (e.g., reflectance times illumination) is approximated by the element-wise product of their latent codes. We show why an exact low-dimensional algebra-preserving code cannot exist for arbitrary spectra when the length k of the latent code is smaller than the number of spectral samples n , and introduce a learned non-negative *linear* encoder-decoder whose architecture makes scaling/addition exact and whose training objective encourages near-multiplicativity under the Hadamard product. With $k = 6$ codes, we render $k/3 = 2$ RGB images per frame using an unmodified RGB renderer, re-assemble the latent image, and decode to high-resolution spectra (or to XYZ/RGB). Experiments in 3D scenes demonstrate that $k = 6$ achieves substantially lower color error than RGB baselines while being significantly faster than naive n -sample spectral rendering; $k = 9$ provides a higher-quality reference. We further introduce a lightweight neural upsampling network that maps RGB assets directly to our compact latent codes, enabling integration of legacy RGB content into the spectral pipeline while maintaining perceptually accurate colors in rendered images.

CCS Concepts: • **Computing methodologies** → **Ray tracing**; **Shading**.

Authors' Contact Information: Jiaqi Yu; Dar'ya Guarnera; Giuseppe Claudio Guarnera, University of York, York, United Kingdom, jiaqi.yu@york.ac.uk, darya.guarnera@york.ac.uk, claudio.guarnera@york.ac.uk.

2026. ACM XXXX-XXXX/2026/2-ART
<https://doi.org/10.1145/nnnnnnn.nnnnnnn>

Additional Key Words and Phrases: spectral rendering, spectral compression, multi-pass rendering, Hadamard algebra, neural codec

ACM Reference Format:

Jiaqi Yu, Dar'ya Guarnera, and Giuseppe Claudio Guarnera. 2026. Compact Hadamard Latent Codes for Efficient Spectral Rendering. 1, 1 (February 2026), 10 pages. <https://doi.org/10.1145/nnnnnnn.nnnnnnn>

1 Introduction

Colour perception in the human visual system originates from electromagnetic radiation in the 380–780 nm range stimulating the short (S), medium (M), and long (L) wavelength cones in the retina [22, 26]. Consequently, colour is not an intrinsic property of light but an interpretation of the Spectral Power Distribution (SPD).

In computer graphics, the RGB model dominates because it is computationally efficient, hardware-friendly, and compact, making it ideal for film visual effects and gaming, particularly real-time rendering [15]. However, three channels are insufficient to encode full spectral information. This limitation results in colour shifts under novel lighting, metamerism artifacts, and an inability to faithfully reproduce wavelength-dependent phenomena such as prismatic dispersion, thin-film interference, and fluorescence [7, 23].

Full spectral rendering addresses these issues by propagating complete spectral distributions through the rendering pipeline. Rather than computing colour as a simple RGB triplet, spectral methods integrate the product of illumination SPD and surface reflectance across all wavelengths before applying colour matching functions: While physically accurate, this approach requires sampling 30–100 wavelengths, inflating computation, storage, and GPU bandwidth. Most rendering pipelines are optimised for RGB workflows, making hardware support for spectral rendering limited [2]. More critically,

the high computational cost significantly hinders real-time applications, restricting spectral rendering to offline use or applications that require accurate results.

The goal of our work is to compress spectra (reflectance, illumination, or their products) into a low-dimensional latent code $\mathbf{z} \in \mathbb{R}^k$ that (i) enables efficient spectral rendering with only a few RGB passes, and (ii) behaves *linearly* under the operations that dominate the rendering equation: scaling, addition (multiple light paths / lights), and element-wise multiplication (material–light interactions).

Given a k -dimensional code per pixel, we can render its components using a standard RGB renderer by packing three code channels into each RGB image. With $k = 6$, this requires $k/3 = 2$ RGB renders per frame: we render two RGB images, re-assemble the resulting k -channel latent image, and then decode it to high-resolution spectra. Figure 1 demonstrates that this approach produces substantially more accurate colors than standard RGB rendering, particularly under challenging narrowband illumination where RGB methods exhibit severe color shifts.

Key Contributions. We first prove that exact, low-dimensional codes preserving all three operations (scaling, addition, Hadamard product) cannot exist for arbitrary spectra, which motivates our distributional learning approach. Our main technical contributions are:

- (1) **Learned linear codec:** A non-negative linear encoder–decoder architecture that exactly preserves scaling/addition and approximately preserves multiplicativity through a multi-objective training procedure, enabling multi-pass rendering with $k/3$ RGB images.
- (2) **Latent upsampling network:** A compact neural network that maps RGB values to our k -dimensional latent codes, enabling integration of legacy RGB assets while maintaining color accuracy via a combined latent-space and perceptual loss formulation.

We provide comprehensive validation in 3D rendering scenarios, showing that $k = 6$ achieves $\sim 23\times$ speedup over full spectral rendering while maintaining substantially lower color error than RGB baselines.

2 Related Work

A variety of spectral compression techniques have been developed to reduce the dimensionality of full spectral data while preserving visually or physically important information.

2.1 Linear Decomposition Methods

Principal Component Analysis (PCA) is one of the earliest and most widely used spectral compression methods. Percy [19] first demonstrated that reflectance and illumination spectra could be projected into a low-dimensional subspace with minimal colorimetric error. Matusik et al. [14] applied PCA to measured BRDFs, enabling compact and editable representations of complex material behaviors. Weyrich et al. [24] further used PCA to analyze the variation of facial appearance parameters in a physically-based skin reflectance model. More recently, Otsu et al. [18] introduced clustered PCA bases for RGB-to-spectral upsampling, achieving better local reconstructions

but with some discontinuities near cluster boundaries. Despite its efficiency, PCA often produces basis functions with negative values and lacks physical interpretability, which can degrade perceptual accuracy under varying lighting.

Non-negative Matrix Factorization (NMF) decomposes spectral data into additive, non-negative components. The non-negativity constraint ensures physically meaningful outputs, aligning with the nature of real-world spectral reflectance. While NMF has been widely adopted in hyperspectral imaging and biomedical applications [5], it is less common in computer graphics due to its iterative optimization and higher computational cost. It often requires more basis vectors than PCA to achieve similar reconstruction accuracy, limiting its use in real-time rendering.

Sparse coding and dictionary learning represent each spectrum as a sparse linear combination of atoms from a learned dictionary. Arad and Ben-Shahar [3] proposed a sparse recovery framework to reconstruct hyperspectral signals from RGB images, achieving better results than PCA, especially for spectra with sharp features. However, sparse models require solving per-input optimization problems and do not generalize well outside the training domain, making them less suitable for interactive rendering.

2.2 Parametric and Perceptual Methods

An alternative to decomposition-based methods is to use parametric models that directly represent smooth, physically valid spectra. Peters et al. [20] proposed using moments to represent bounded signals for spectral rendering. Their method uses Fourier coefficients combined with a bounded maximum entropy spectral estimate, achieving compact representation with 3-8 coefficients while maintaining smooth, energy-conserving spectra. This approach addresses the ringing artifacts of truncated Fourier series and ensures all reconstructed albedos remain between zero and one.

Several methods exploit the connection between spectra and human color perception. Karimipour et al. [12] proposed encoding reflectance spectra as 3×3 matrices through least-squares fitting to cone response functions, achieving perceptually accurate reconstruction under broadband illumination ($\Delta E_{94} < 1$). However, this approach shows significant limitations under narrowband lighting (ΔE_{94} up to 16) and requires matrix operations that are awkward to integrate into vector-based renderers. Our work addresses these limitations by learning compact vector codes that maintain accuracy across diverse lighting conditions.

2.3 RGB-to-Spectrum Upsampling and Spectral Sampling

Converting RGB texture assets to plausible spectral distributions is critical for spectral rendering pipelines. Meng et al. [16] introduced a physically meaningful approach covering nearly the entire XYZ color space. Jakob and Hanika [9] presented a breakthrough low-dimensional parametric model achieving zero error on the full sRGB gamut while requiring only three coefficients. Their method uses smooth, energy-conserving basis functions and has been adopted in production renderers including PBRT [21] and Mitsuba [17]. Extensions have addressed wide-gamut color spaces through fluorescent components [10], one-to-many upsampling for metameric effects [4], and specialized techniques for upsampling illumination spectra [7].

Efficient Monte Carlo spectral sampling requires minimizing variance from stochastic wavelength selection. Wilkie et al. [25] introduced hero wavelength sampling, which samples a primary “hero” wavelength for path construction while placing additional wavelengths at regular intervals. This approach reduces color noise compared to single-wavelength sampling while maintaining spectral accuracy for phenomena like subsurface scattering and dispersion, and has been adopted in production rendering.

2.4 Neural and Learning-Based Approaches

Neural networks offer the potential for non-linear compressions that capture complex spectral patterns beyond linear models. Kang et al. [11] developed an asymmetric autoencoder for BRDF capture, allowing accurate reconstruction from limited measurements. Their differentiable approach supports integration with neural rendering frameworks, though it requires large datasets and additional constraints to enforce physical properties.

More recently, Li et al. [13] introduced SpectralNeRF, combining neural radiance fields with physically-based spectral rendering. Their MLP-based architecture (SpectralMLP) constructs spectral radiance fields with a Spectrum Attention UNet (SAUNet) to generate RGB outputs, demonstrating superior performance for wavelength-dependent effects. However, SpectralNeRF operates at the scene level rather than providing a general spectral compression codec suitable for arbitrary rendering pipelines.

2.5 Our Approach

While existing methods offer various trade-offs between accuracy, efficiency, and interpretability, none are fully optimized for real-time spectral rendering under variable illumination with integration into standard RGB rendering pipelines. Linear decomposition methods like PCA lack physical constraints and can produce negative values. Parametric methods like moment-based representations [20] or perceptual matrices [12] either focus on single spectral types or struggle with narrowband illumination. Neural scene representations like SpectralNeRF [13] are scene-specific rather than general-purpose codecs.

Our contribution is a learned linear codec that: (1) guarantees exact scaling and addition through its architecture, (2) approximates multiplicativity via specialized training, (3) maintains non-negativity for physical plausibility, (4) achieves robust performance across broadband and narrowband illumination, and (5) integrates seamlessly into standard RGB rendering pipelines by treating latent codes as RGB triplets across multiple passes. This bridges the gap between efficient RGB workflows and accurate spectral rendering.

3 Renderer-Friendly Latent Codes

For fast rendering, we require a representation that composes under the same algebra as the rendering equation. In path tracing, spectral quantities are repeatedly:

- (1) **Scaled:** Light intensity modulation, BSDF evaluation.
- (2) **Added:** Multiple light contributions, path accumulation.
- (3) **Multiplied element-wise:** Reflectance \times illumination at each wavelength.

This motivates a code space that supports these operations directly on compact codes, enabling reuse of existing RGB infrastructure.

3.1 Why Exact Algebra-Preserving Compression is Impossible

Let \mathbb{R}^n denote discretised spectra (e.g., $n = 47$ uniformly spaced wavelength samples in the 368–830 nm range) equipped with standard addition and the Hadamard (element-wise) product, forming an algebra $(\mathbb{R}^n, +, \odot)$.

Suppose we seek a codec with encoder $E : \mathbb{R}^n \rightarrow \mathbb{R}^k$ and decoder $D : \mathbb{R}^k \rightarrow \mathbb{R}^n$ that preserves all three operations exactly for *arbitrary* spectra:

$$E(\alpha s) = \alpha E(s) \quad (\text{scaling}) \quad (1)$$

$$E(s_1 + s_2) = E(s_1) + E(s_2) \quad (\text{addition}) \quad (2)$$

$$E(s_1 \odot s_2) = E(s_1) \odot E(s_2) \quad (\text{Hadamard product}) \quad (3)$$

If such a codec existed with $k < n$, then E would be an algebra homomorphism from $(\mathbb{R}^n, +, \odot)$ to $(\mathbb{R}^k, +, \odot)$.

Algebraic Obstruction. The algebra $(\mathbb{R}^n, +, \odot)$ is isomorphic to the direct product of n copies of \mathbb{R} . Any homomorphism to $(\mathbb{R}^k, +, \odot)$ must map each coordinate independently. For $k < n$, this means the map cannot be injective—multiple distinct spectra would map to the same code. More strongly, exact preservation of Hadamard products implies that the encoder must essentially be a coordinate projection, which provides no meaningful compression for arbitrary spectra.

Distributional Goal. Therefore, our goal shifts from exact algebra preservation for *all* spectra to *approximate* preservation for the *distribution of spectra encountered in rendering*. Natural reflectance and illumination spectra occupy a low-dimensional manifold within \mathbb{R}^n ; we exploit this structure to learn codes that behave approximately algebraically on this manifold.

4 Learned Non-Negative Linear Hadamard Codec

4.1 Architecture Overview

Design Rationale. As discussed in Section 3.1, exact preservation of all three operations (scaling, addition, and multiplication) in a compressed code space is algebraically impossible. We therefore adopt a deliberate compromise: our architecture *exactly* preserves scaling and addition through linearity, while *approximately* enforcing multiplicativity through training objectives. This design choice is motivated by the structure of path tracing, where additions of light contributions (from multiple light sources, multiple paths, and light transport accumulation) are ubiquitous at every bounce, whereas element-wise multiplication primarily occurs at surface interactions. Exact linearity ensures that the fundamental superposition principle of light transport is preserved without accumulated drift, while learned approximate multiplicativity suffices for material–light interactions where small deviations are perceptually tolerable.

Furthermore, we employ a *single* encoder–decoder pair for both reflectance and illumination spectra. This unified representation ensures that both spectral types are embedded into the same latent space, which is essential for the blockwise Hadamard product (Section 4.2) to approximate the spectral product $s_R \odot s_L$ in latent space.

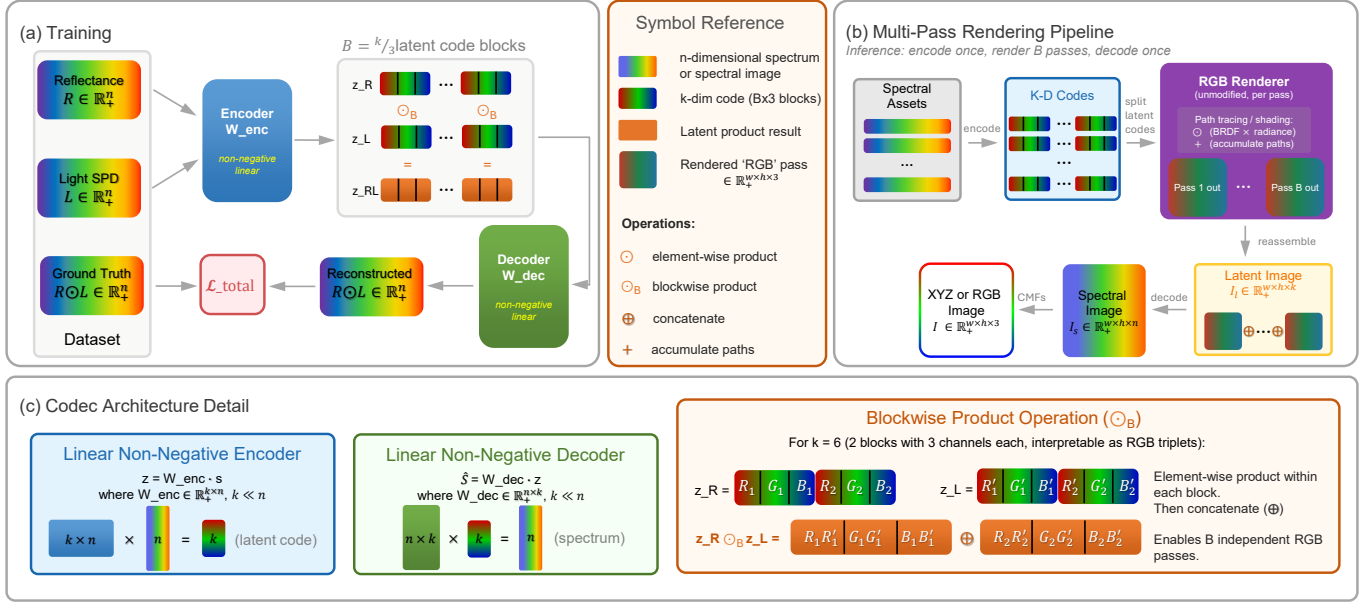


Fig. 2. Overview of our learned Hadamard spectral codec and multi-pass rendering pipeline. **(a) Training:** The encoder \mathcal{E} (with weights W_{enc}) maps reflectance R and illumination L spectra to k -dimensional latent codes, which are split into $B = k/3$ blocks. These codes undergo a blockwise Hadamard product \odot_B , and the decoder \mathcal{D} (with weights W_{dec}) reconstructs the spectral product $R \odot L$. The multi-objective loss $\mathcal{L}_{\text{total}}$ enforces reconstruction fidelity and near-multiplicativity. **(b) Multi-Pass Rendering Pipeline:** At inference time, spectral assets are encoded once into k -dimensional codes. Each code is partitioned into B RGB-like triplets, which are rendered independently using an unmodified RGB renderer across B passes. The outputs are reassembled into a latent image and decoded once to produce the final spectral or XYZ/RGB image. **(c) Codec Architecture Detail:** The encoder and decoder are linear transformations with non-negative weights. The blockwise product operation \odot_B performs element-wise multiplication within each 3-channel block, enabling B independent rendering passes that approximate the spectral product in compressed space.

Training a single codec on both spectral types naturally encourages the learned basis to capture the shared low-dimensional structure underlying natural spectra, rather than overfitting to one category.

Linear Non-Negative Encoder–Decoder. We use a linear encoder and decoder (Figure 2a,c):

$$z = E(s) = W_{\text{enc}} s, \quad \hat{s} = D(z) = W_{\text{dec}} z, \quad (4)$$

where $W_{\text{enc}} \in \mathbb{R}^{k \times n}$ and $W_{\text{dec}} \in \mathbb{R}^{n \times k}$.

Crucially, both weight matrices are constrained to be *non-negative* by parameterising them through a softplus function:

$$W = \text{softplus}(\tilde{W}) = \frac{1}{\beta} \log(1 + e^{\beta \tilde{W}}) \quad (5)$$

where \tilde{W} are the learnable parameters and $\beta = 10$ controls sharpness.

Linearity guarantees $E(\alpha s) = \alpha E(s)$ and $E(s_1 + s_2) = E(s_1) + E(s_2)$ by construction. Non-negative weights ensure that latent codes remain non-negative for non-negative spectra, and decoded spectra cannot be negative. The decoder columns can be interpreted as basis spectra, with latent codes representing their non-negative mixture weights.

4.2 Blockwise Hadamard Product

We choose $k = 3B$ so that codes split into B blocks of 3 channels, enabling direct interpretation as RGB triplets for rendering (Figure 2c).

For two spectra s_R (reflectance) and s_L (illumination), we define the *blockwise Hadamard product*:

$$z_{RL} = E(s_R) \odot_B E(s_L) = \bigoplus_{i=1}^B \left(z_R^{(i)} \odot z_L^{(i)} \right) \quad (6)$$

where $z^{(i)} \in \mathbb{R}^3$ denotes the i -th sub-block and \oplus represents concatenation.

This design constrains the network to learn decoupled spectral bases that mimic the algebraic properties of high-dimensional spectral multiplication within each trichromatic-like block. The key insight is that, rather than requiring exact equality, we *approximate*:

$$E(s_R \odot s_L) \approx E(s_R) \odot_B E(s_L) \quad (7)$$

4.3 Training Objectives

We train the codec using a multi-objective loss function:

$$\mathcal{L}_{\text{total}} = \lambda_{e2e} \mathcal{L}_{e2e} + \lambda_{\text{rec}} \mathcal{L}_{\text{rec}} + \lambda_{\text{code}} \mathcal{L}_{\text{code}} + \lambda_{\text{col}} \mathcal{L}_{\text{col}} \quad (8)$$

End-to-End Reconstruction Loss. The primary objective minimises discrepancy between the reconstructed spectral radiance and the ground-truth product:

$\mathcal{L}_{e2e} = \text{MSE}(\hat{S}, R \odot L) \cdot (2 - \cos(\hat{S}, R \odot L))$, where $\hat{S} = D(E(R) \odot_B E(L))$. The cosine similarity term ensures both magnitude and spectral shape are captured.

Reconstruction Loss. To ensure the encoder/decoder generalises across spectral types: $\mathcal{L}_{\text{rec}} = \text{MSE}(D(E(R)), R) + \text{MSE}(D(E(L)), L)$.

Latent Multiplicativity Loss. To enforce algebraic properties in the compressed domain: $\mathcal{L}_{\text{code}} = \text{MSE}(E(R) \odot_B E(L), E(R \odot L))$. This encourages the blockwise product of codes to match the code of the product.

Colour-Aware Loss. To align reconstruction with human visual perception, following [6]: $\mathcal{L}_{\text{col}} = \text{MSE}(T_{\text{cmf}}\hat{S}, T_{\text{cmf}}(R \odot L))$, where $T_{\text{cmf}} \in \mathbb{R}^{3 \times n}$ contains the CIE colour matching functions.

Non-negativity Constraints. Non-negative outputs are guaranteed by the architecture: since both W_{enc} and W_{dec} are constrained to be non-negative via softplus, and input spectra are physically non-negative, all intermediate codes and decoded spectra remain non-negative through matrix multiplication and element-wise products.

4.4 Dataset

To learn effective spectral encoding and decoding, our training data comprises reflectance and illumination spectra covering diverse chromaticities. Both datasets use 47 equally spaced wavelength samples spanning 368–830 nm (zeroed outside 400–700 nm) and are split 70/30 into training and test sets using adaptive concentric rings in CIELAB a^*b^* space to ensure representative coverage across hues and saturations. A validation subset is randomly drawn from the training set for hyperparameter tuning; the test is set fully held out.

Reflectances. We begin with 1,269 measured reflectance spectra from the Munsell color system. To extend coverage toward highly saturated colors underrepresented in natural surfaces, we augment with two sets of synthetic spectra: (i) 36 optimal reflectances targeting sRGB primaries via bounded least-squares at $s \in [0.6, 0.98]$ and $Y = 0.30 \cdot Y_{\text{max}}$, and (ii) 144 smooth spectral reflectances generated using basis-function optimization with 24 hue directions and 6 saturation levels ($s \in [0.7, 0.98]$). For each sRGB primary target, we solve:

$$\min_r \left\| \begin{bmatrix} w_X \\ w_Y \\ w_Z \end{bmatrix}^\top r - \begin{bmatrix} X_t \\ Y_t \\ Z_t \end{bmatrix} \right\|^2 \quad \text{s.t. } w_Y^\top r = Y_0, \quad 0 \leq r \leq 1, \quad (9)$$

where w_X, w_Y, w_Z are per-wavelength D65-weighted XYZ basis vectors and (X_t, Y_t, Z_t) is the target tristimulus. All 1,449 reflectances are resampled to 47 wavelengths and split using 180 angular bins, computing ring boundaries adaptively per angle via quantile thresholds of the radial distance from the dataset’s median a^*b^* center. Within each ring-sector cell, we randomly allocate 70% of spectra to training and 30% to testing. This strategy avoids spatial clustering artifacts and ensures both sets span the full range of hues and saturations, yielding 1,013 training and 436 test spectra. In the supplementary material we report representative reflectance spectra from the test set and their chromaticity coordinates within the CIE xy diagram.

Illuminations. Our illumination dataset combines multiple sources: measured lamp spectra from the LSPDD database [1] (compact fluorescent, halogen, LED, metal halide, incandescent, standard illuminants), simulated CIE daylight spectra, 82 synthetic broadband spectra with varying CCTs, and 367 narrowband spectra with sharp

spectral features. We augment the filtered set with vertically flipped versions of broadband spectra (which simulate inverted spectral shapes), to enrich spectral shape diversity, then merge with daylight and narrowband sources. To reduce redundancy, we apply iterative greedy filtering based on cosine similarity with threshold $\tau=0.95$: we select spectra ensuring no pair has similarity $\geq \tau$. After normalization to unit peak and resampling to 47 wavelengths, the curated dataset contains 708 spectra, split into training and test using 36 angular bins. During training, we apply scaling augmentation to improve robustness. Representative illumination spectra from the test are reported in the supplementary material.

4.5 Hyperparameter Selection via Multi-Bounce Ablation

Because our target use case is path tracing, we select hyperparameters based on how well the codec preserves multiplicative structure over *cascaded* reflectance–radiance interactions. Single-interaction reconstruction losses do not capture this error propagation, so we use a simple multi-bounce proxy that repeatedly applies element-wise products and measures the resulting colour error.

Grid Search Methodology. We performed a grid search over the loss weights $\lambda_{\text{rec}} \in (0 : 0.5 : 3.0)$, $\lambda_{e2e} \in (0 : 0.5 : 2.0)$, $\lambda_{\text{code}} \in (0 : 0.25 : 1.0)$, and $\lambda_{\text{col}} \in (0 : 0.25 : 1.0)$, yielding 700 codec variants. All runs used the same data, architecture, and optimisation settings (Adam, lr= 10^{-3} , batch size 128, up to 150 epochs with early stopping, patience 15).

Multi-Bounce Evaluation Protocol. For each trained codec, we evaluate a synthetic b -bounce chain on 500 test reflectance–illumination pairs by repeatedly multiplying by newly sampled reflectances:

$$S^{(1)} = R^{(1)} \odot L; \quad S^{(2)} = R^{(2)} \odot S^{(1)}; \quad S^{(3)} = R^{(3)} \odot S^{(2)}. \quad (10)$$

We compute the same recurrence in latent space using the blockwise Hadamard product \odot_B , and compare to the ground-truth spectral chain via perceptual CIE94 ΔE . This directly tests whether the codec remains accurate under repeated multiplicative composition.

Hadamard Algebra Regularisation. We also tested an auxiliary algebra regulariser encouraging decoder columns \mathbf{b}_i to be approximately Hadamard-orthogonal ($\mathbf{b}_i \odot \mathbf{b}_j \approx \mathbf{0}$ for $i \neq j$) and idempotent ($\mathbf{b}_i \odot \mathbf{b}_i \approx \mathbf{b}_i$), with $\lambda_{\text{alg}} \in (0.001 : 0.004 : 0.01)$ [3]. This produced no measurable improvement in either reconstruction or multi-bounce error, so we set $\lambda_{\text{alg}}=0$ in all reported results. We hypothesise that the combination of \mathcal{L}_{e2e} , $\mathcal{L}_{\text{code}}$, and non-negativity constraints already guide the network toward a factorizable basis structure, and the explicit blockwise product architecture inherently biases the learned representation toward the desired algebraic properties.

Selected Configuration. From the 700 variants, we choose the setting that performs robustly across 1–3 bounces, achieving mean CIE94 errors of $\Delta E=2.16$ ($S^{(1)}$), 1.79 ($S^{(2)}$), and 1.74 ($S^{(3)}$): $\lambda_{e2e}=0.5$, $\lambda_{\text{rec}}=0.75$, $\lambda_{\text{code}}=1.0$, $\lambda_{\text{col}}=0.5$.

5 Latent Upsampling from RGB Assets

While our spectral codec enables efficient rendering from spectral data, real-world production pipelines often contain extensive libraries of RGB textures, materials, and assets. To enable integration of such legacy content into our spectral rendering framework, we

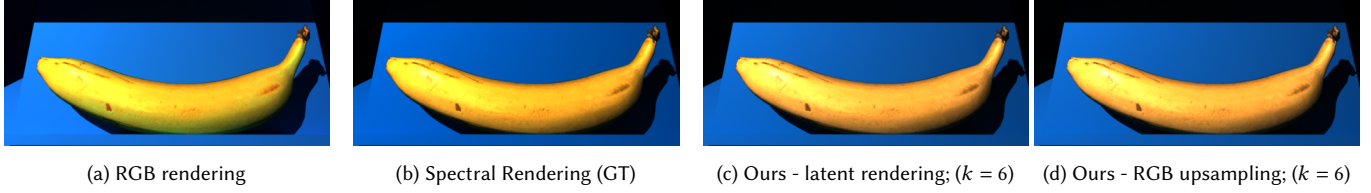


Fig. 3. Comparison of rendering methods on textured objects: (a) standard RGB rendering, (b) full spectral ground truth, (c) our $k=6$ latent rendering, and (d) RGB textures and lights upsampled to $k=6$ codes. Our native latent rendering (c) matches ground truth (b), while upsampled RGB assets (d) achieve significantly better color accuracy than RGB rendering (a), as visible in the banana and blue sample holder. This demonstrates integration of RGB assets via latent upsampling, so that legacy RGB content can benefit from spectral rendering accuracy without requiring spectral source data.

introduce a lightweight *latent upsampling network* that maps RGB values directly to our compact k -dimensional latent codes. This approach leverages the spectral manifold learned by the pretrained codec rather than attempting ill-posed direct RGB-to-spectrum reconstruction.

5.1 Architecture

The upsampling network is a compact multilayer perceptron that takes a 3-channel RGB input and predicts a k -dimensional latent vector:

$$\mathbf{z}_{\text{pred}} = f_{\theta}(\mathbf{c}_{\text{RGB}}) \quad (11)$$

where f_{θ} consists of three fully connected layers with hidden dimensions of 128 and SiLU activations. Importantly, the network operates strictly per-pixel without spatial coupling, as the upsampling task is fundamentally color-driven rather than texture-dependent. This design keeps the model numerically stable, computationally efficient, and applicable to both uniform colors and spatially varying RGB textures.

The predicted latent codes are subsequently decoded into full spectral representations using the fixed, pretrained spectral decoder from our linear codec (Section 4). By predicting in the learned latent space rather than directly in the n -dimensional spectral space, the network benefits from the codec’s prior knowledge of physically plausible spectral distributions.

5.2 Training Dataset and Objective

The upsampling network is trained on the same dataset used for codec training (Section 4.4), comprising 1,013 training spectra. For each spectral sample s , we compute its linear RGB representation \mathbf{c}_{RGB} and the corresponding ground-truth latent code $\mathbf{z}_{\text{gt}} = \mathbb{E}(s)$ using the pretrained encoder.

The training objective combines two complementary terms:

$$\mathcal{L}_{\text{upsample}} = \mathcal{L}_{\text{latent}} + \lambda_{\text{color}} \cdot \mathcal{L}_{\text{color}} \quad (12)$$

The primary loss enforces consistency in the learned latent space, combining MSE with a maximum absolute error penalty to control worst-case deviations:

$$\mathcal{L}_{\text{latent}} = \text{MSE}(\mathbf{z}_{\text{pred}}, \mathbf{z}_{\text{gt}}) + \lambda_{\text{maxabs}} \cdot \mathbb{E} \left[\max_i |z_{\text{pred}}^{(i)} - z_{\text{gt}}^{(i)}| \right] \quad (13)$$

where the maximum is taken over latent dimensions i for each sample, and we use $\lambda_{\text{maxabs}}=0.3$. This combined formulation encourages both overall reconstruction accuracy and tight control of outlier errors across all latent dimensions.

Perceptual Color Loss. To ensure perceptual color stability after decoding and rendering, we add a color-space supervision term. The predicted and ground-truth latent codes are decoded to spectra using the fixed decoder $D(\cdot)$, converted to CIE XYZ tristimulus values via color matching functions, and transformed to CIE Lab space to compute the ΔE_{76} color difference:

$$\mathcal{L}_{\text{color}} = \Delta E_{76}(\text{Lab}(C(D(\mathbf{z}_{\text{pred}}))), \text{Lab}(C(D(\mathbf{z}_{\text{gt}})))) \quad (14)$$

where $C(\cdot)$ denotes the spectral-to-XYZ colorimetric projection and $\text{Lab}(\cdot)$ is the standard nonlinear XYZ-to-Lab transformation. We use $\lambda_{\text{color}}=0.05$.

By combining latent-space consistency with perceptual color supervision, this formulation encourages the network to predict latent codes that remain on the learned spectral manifold while simultaneously ensuring perceptually accurate color reproduction. The relatively low weight on the color loss ($\lambda_{\text{color}}=0.05$) reflects the fact that the latent loss already provides strong spectral guidance; the color term primarily serves to suppress unstable outliers.

Training Details. The network is trained using AdamW optimization with learning rate 2×10^{-3} , weight decay 10^{-5} , batch size 64, and gradient clipping at norm 1.0. We employ a ReduceLROnPlateau scheduler (factor 0.5, patience 200 epochs, minimum lr 10^{-6}) and train for 4,500 epochs. The pretrained $k = 6$ codec weights (from Section 4) are frozen during upsampling network training.

6 Experiments

We evaluate our Hadamard spectral codes using 47-channel spectral rendering as ground truth, and compare against standard RGB rendering and latent multi-pass rendering. Unless otherwise stated, we report our main configuration $k=6$ (two RGB passes), and use $k=9$ as a higher-quality reference (three RGB passes). All qualitative figures decode latent images to spectra and then convert to sRGB for visualization. Additional quantitative tables and ablations are provided in the supplemental.

6.1 Renderer Integration

Our codec integrates into an unmodified RGB path tracer by packing the k -dimensional latent code into $B=k/3$ RGB triplets and rendering B passes (Fig. 2b). We use Mitsuba v0.6 [8] with full spectral support for ground truth and the standard RGB variant for latent rendering. With $k=6$, only two RGB passes are required.

6.2 Results: Reconstruction Quality

Legacy RGB assets via latent upsampling. We first evaluate the RGB-to-latent upsampling network (Section 5) on a textured scene (Fig. 3) and on a Cornell box containing diverse BRDFs and a ColorChecker chart under broadband illumination (Fig. 4). In both cases, upsampled RGB materials and lights rendered through our pipeline are visually close to the spectral ground truth and substantially outperform standard RGB rendering.

Spectral smoothness of upsampled codes. While colorimetric accuracy is generally preserved, the upsampling network does not explicitly enforce spectral smoothness. Figure 7 shows per-patch spectra for a ColorChecker chart, where some reconstructed spectra (dashed) exhibit non-smooth or spiky artifacts compared to the ground truth (solid). This issue arises from using a single network to upsample both reflectance and illumination.

Stress test: spiky narrowband illumination. Figure 5 evaluates the same Cornell box scene under spiky, narrowband LED illumination. The $k=6$ configuration preserves overall color relationships, while $k=9$ further reduces residual error, as shown by the per-pixel MSE maps (Fig. 5d,f), providing a higher-quality reference at the cost of one additional RGB pass.

Complex material interactions. Figure 6 shows a refractive glass scene with strong multi-layer light transport. Despite multiple material interactions and refraction, our $k=6$ latent rendering remains visually close to the spectral ground truth under both broadband and narrowband illumination.

6.3 Results: Multi-Bounce Stability

A key motivation for Hadamard spectral codes is robustness under repeated reflectance–radiance products. We therefore evaluate error propagation with increasing bounce count. Figure 8 shows 1, 2, 3, and unbounded-depth path tracing under broadband illumination. The per-pixel MSE increases slightly from one to two bounces and then stabilizes, indicating that the approximate Hadamard product does not lead to runaway error at typical indoor path depths. Corresponding narrowband multi-bounce results are included in the supplemental.

6.4 Results: Performance

With $k=6$, our method requires only two RGB render passes instead of 47 spectral samples, yielding a $\sim 23\times$ reduction in render passes. The encoder and decoder are small linear transforms applied once per frame, adding negligible overhead compared to rendering.

7 Conclusion

We introduced *Hadamard spectral codes*, a learned, non-negative, linear spectral representation that enables efficient spectral rendering using a small number of standard RGB passes. By enforcing exact scaling and addition in latent space and encouraging approximate multiplicativity under the Hadamard product, our method integrates seamlessly into existing RGB rendering pipelines.

Across a range of 3D scenes, materials, and lighting conditions (Figs. 3–8), we showed that $k=6$ codes (two RGB passes) achieve

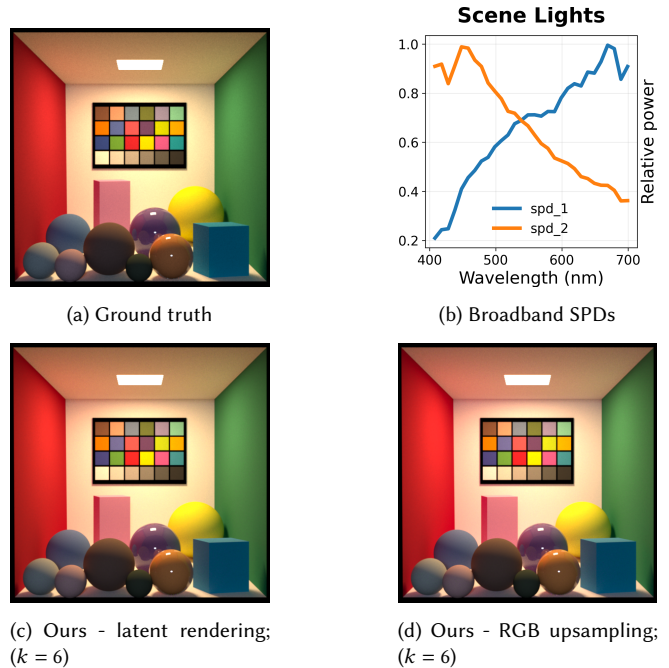


Fig. 4. Cornell box scene with diverse materials and broadband illumination. (a) Ground truth spectral rendering showing a color checker chart, diffuse walls, and objects with varied BRDFs. (b) Two broadband illuminant SPDs used in the scene (warm and cool). (c) Our native $k=6$ latent rendering produces results visually indistinguishable from ground truth. (d) RGB assets (materials, textures, lights) upsampled to $k=6$ latent codes and rendered through our pipeline also achieve visually accurate color reproduction.

visually accurate results under both broadband and challenging narrowband illumination, while remaining stable under multi-bounce light transport. A higher-dimensional setting ($k=9$) provides a useful quality reference at modest additional cost. We further demonstrated that legacy RGB assets can be incorporated via a lightweight RGB-to-latent upsampling network.

Our approach has several limitations. Because multiplicativity is only approximated, errors are most visible under extremely spiky spectra and after many light interactions. In addition, the current RGB-to-latent upsampling network does not explicitly enforce spectral smoothness, and can produce non-smooth reconstructed spectra (Fig. 7). This is likely due to using a single network for both reflectance and illumination; exploring separate upsamplers and smoothness-aware losses is an important direction for future work.

Overall, Hadamard spectral codes bridge the gap between efficient RGB workflows and physically motivated spectral rendering, enabling practical spectral effects in production-oriented rendering systems.

References

- [1] 2026. Lamp Spectral Power Distribution Database (LSPDD). <https://lspdd.org/>. Accessed: 2026-01-22.
- [2] Tomas Akenine-Mller, Eric Haines, and Naty Hoffman. 2018. Real-Time Rendering, 4th. USA: AK Peters, Ltd (2018), 36–38.
- [3] Boaz Arad and Ohad Ben-Shahar. 2016. Sparse Recovery of Hyperspectral Signal from Natural RGB Images. In *Computer Vision – ECCV 2016*. Springer, 19–34. doi:10.1007/978-3-319-46478-7_2
- [4] Laurent Belcour, Pascal Barla, and Gaël Guennebaud. 2023. One-to-Many Spectral Upsampling of Reflectances and Transmittances. *Computer Graphics Forum* 42, 4 (2023). doi:10.1111/cgf.14886 Proceedings of Eurographics Symposium on Rendering.
- [5] Michael W. Berry, Murray Browne, Amy N. Langville, V. Paul Pauca, and Robert J. Plemmons. 2007. Algorithms and Applications for Approximate Nonnegative Matrix Factorization. *Computational Statistics & Data Analysis* 52, 1 (2007), 155–173. doi:10.1016/j.csda.2006.11.006
- [6] CIE. 2019. Colour-matching functions of CIE 1931 standard colorimetric observer. doi:10.25039/CIE.DS.xvudnb9b International Commission on Illumination (CIE), Vienna, Austria.
- [7] Giuseppe Claudio Guarnera, Yuliya Gitlina, Valentin Deschaintre, and Abhijeet Ghosh. 2022. Spectral Upsampling Approaches for RGB Illumination. In *Proceedings of Eurographics Symposium on Rendering*. doi:10.2312/sr.20221153
- [8] Wenzel Jakob. 2010. Mitsuba renderer. <http://www.mitsuba-renderer.org>.
- [9] Wenzel Jakob and Johannes Hanika. 2019. A Low-Dimensional Function Space for Efficient Spectral Upsampling. *Computer Graphics Forum* 38, 4 (2019), 147–155. doi:10.1111/cgf.13626 Proceedings of Eurographics Symposium on Rendering.
- [10] Alisa Jung, Alexander Wilkie, Johannes Hanika, Wenzel Jakob, and Carsten Dachsbacher. 2019. Wide Gamut Spectral Upsampling with Fluorescence. *Computer Graphics Forum* 38, 4 (2019), 87–96. doi:10.1111/cgf.13773 Proceedings of Eurographics Symposium on Rendering.
- [11] Kaizhang Kang, Zimin Chen, Jiaping Wang, Kun Zhou, and Hongzhi Wu. 2018. Efficient Reflectance Capture using an Autoencoder. *ACM Transactions on Graphics* 37, 4, Article 127 (2018). doi:10.1145/3197517.3201375
- [12] Hamed Karimipour, J. Kevin O'Regan, and Christoph Witzel. 2023. Sensory Representation of Surface Reflectances: Assessments with Hyperspectral Images. *Journal of the Optical Society of America A* 40, 3 (March 2023), A183–A189. doi:10.1364/JOSAA.477501
- [13] Ru Li, Jia Liu, Guanghui Liu, Shengxi Zhang, Bing Zeng, Shuaicheng Liu, Matthew Wooldridge, Jennifer Dy, and Srinivasan Natarajan. 2024. SpectralNeRF: Physically Based Spectral Rendering with Neural Radiance Field. In *Proceedings of the Thirty-Eighth AAAI Conference on Artificial Intelligence*. 3154–3162. doi:10.1609/aaai.v38i4.28099
- [14] Wojciech Matusik. 2003. *A Data-Driven Reflectance Model*. Ph. D. Dissertation. Massachusetts Institute of Technology.
- [15] Johannes Meng, Florian Simon, Johannes Hanika, and Carsten Dachsbacher. 2015. Physically meaningful rendering using tristimulus colours. In *Computer Graphics Forum*, Vol. 34. Wiley Online Library, 31–40.
- [16] Johannes Meng, Florian Simon, Johannes Hanika, and Carsten Dachsbacher. 2015. Physically Meaningful Rendering using Tristimulus Colours. *Computer Graphics Forum* 34, 4 (2015), 31–40. doi:10.1111/cgf.12676 Proceedings of Eurographics Symposium on Rendering.
- [17] Merlin Nimier-David, Delio Vicini, Tizian Zeltner, and Wenzel Jakob. 2019. Mitsuba 2: A Retargetable Forward and Inverse Renderer. *ACM Transactions on Graphics* 38, 6, Article 203 (2019). doi:10.1145/3355089.3356498 Proceedings of SIGGRAPH Asia.
- [18] Hisanari Otsu, Masafumi Yamamoto, and Toshiya Hachisuka. 2018. Reproducing Spectral Reflectances from Tristimulus Colours. *Computer Graphics Forum* 37, 6 (2018), 370–381. doi:10.1111/cgf.13332
- [19] Mark S. Peercy. 1993. Linear Color Representations for Full Speed Spectral Rendering. In *Proceedings of the 20th Annual Conference on Computer Graphics and Interactive Techniques (SIGGRAPH '93)*. 191–198. doi:10.1145/166117.166143
- [20] Christoph Peters, Sebastian Merzbach, Johannes Hanika, and Carsten Dachsbacher. 2019. Using Moments to Represent Bounded Signals for Spectral Rendering. *ACM Transactions on Graphics* 38, 4, Article 136 (2019). doi:10.1145/3306346.3322964
- [21] Matt Pharr, Wenzel Jakob, and Greg Humphreys. 2016. *Physically Based Rendering: From Theory to Implementation* (third ed.). Morgan Kaufmann, San Francisco, CA. <https://pbrt.org/>
- [22] Evan Thompson, Adrian Palacios, and Francisco J Varela. 1992. On the ways to color. *Behavioral and Brain Sciences* 15, 1 (1992), 56–74.
- [23] Shin Watanabe, Shota Kanamori, Sho Ikeda, Bisser Raytchev, Toru Tamaki, and Kazufumi Kaneda. 2013. Performance Improvement of Physically Based Spectral Rendering using Stochastic Sampling. In *Computational Color Imaging: 4th International Workshop, CCIW 2013*. Springer, 184–198. doi:10.1007/978-3-642-36700-7_15
- [24] Tim Weyrich, Wojciech Matusik, Hanspeter Pfister, Bernd Bickel, Craig Donner, Chien Tu, Janet McAndless, Jinho Lee, Addy Ngan, Henrik Wann Jensen, and Markus Gross. 2006. Analysis of Human Faces Using a Measurement-Based Skin Reflectance Model. *ACM Transactions on Graphics* 25, 3 (2006), 1013–1024. doi:10.1145/1141911.1141987
- [25] Alexander Wilkie, Sehera Nawaz, Marc Droske, Andrea Weidlich, and Johannes Hanika. 2014. Hero Wavelength Spectral Sampling. *Computer Graphics Forum* 33, 4 (2014), 123–131. doi:10.1111/cgf.12419 Proceedings of Eurographics Symposium on Rendering.
- [26] Semir Zeki. 1983. Colour coding in the cerebral cortex: the reaction of cells in monkey visual cortex to wavelengths and colours. *Neuroscience* 9, 4 (1983), 741–765.

A Additional Rendering Results

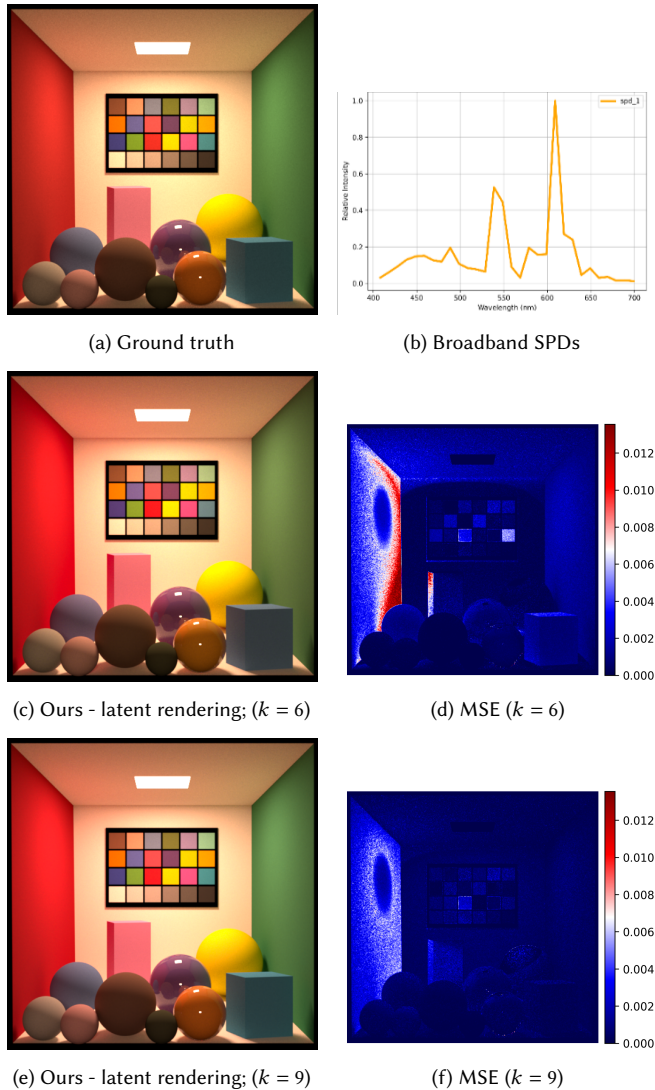


Fig. 5. Cornell box scene with diverse materials under broadband illumination. (a) Ground truth spectral rendering showing a color checker chart, diffuse walls, and objects with varied BRDFs. (b) Broadband illuminant SPDs used in the scene. (c) Our native $k=6$ latent rendering with (d) corresponding per-pixel MSE error map. (e) Our native $k=9$ latent rendering with (f) corresponding per-pixel MSE error map. While $k=9$ produces lower reconstruction error (mean MSE: [value]), the more practical $k=6$ configuration still achieves perceptually accurate results suitable for production rendering.

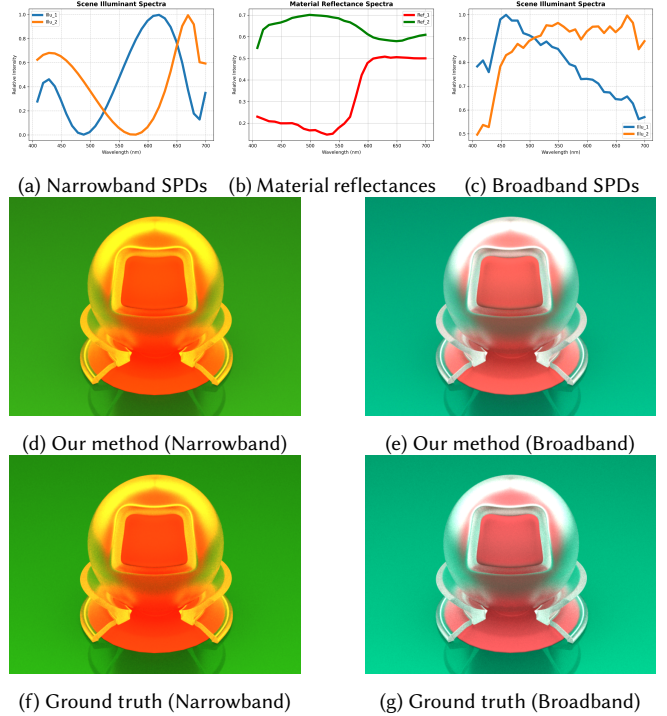


Fig. 6. Glass material rendering with multi-layer light transport. The scene features a glass outer shell containing colored internal objects (object by Jonas Pilo). **Top row:** Spectral input data—(a) narrowband SPDs, (b) reflectances of plane and inner object, (c) broadband SPDs. **Middle row:** Our $k=6$ results under (d) narrowband and (e) broadband illumination. **Bottom row:** Ground truth renderings (f–g). Despite the complex light paths through refractive glass and multiple material interactions, our method achieves visually accurate results under both challenging narrowband and smooth broadband illumination conditions.

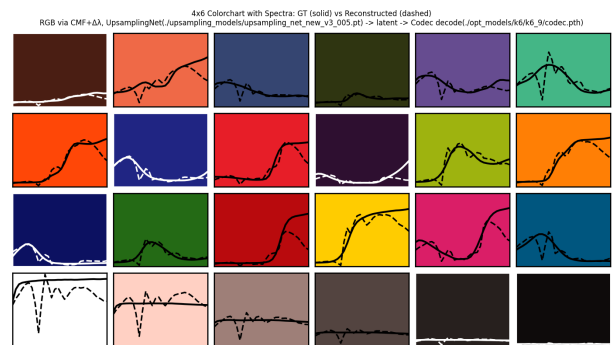


Fig. 7. Spectral reconstruction behaviour of the RGB-to-latent upsampling network on a 4x6 ColorChecker chart. Each tile shows one patch; solid curves denote ground-truth spectra, while dashed curves denote spectra reconstructed by RGB-to-latent upsampling followed by our linear decoder. While the resulting colors are typically accurate, some reconstructed spectra exhibit non-smooth or spiky artifacts. This highlights a limitation of using a single upsampling network for both reflectance and illumination, and motivates future work on separate upsamplers and explicit spectral smoothness regularization.

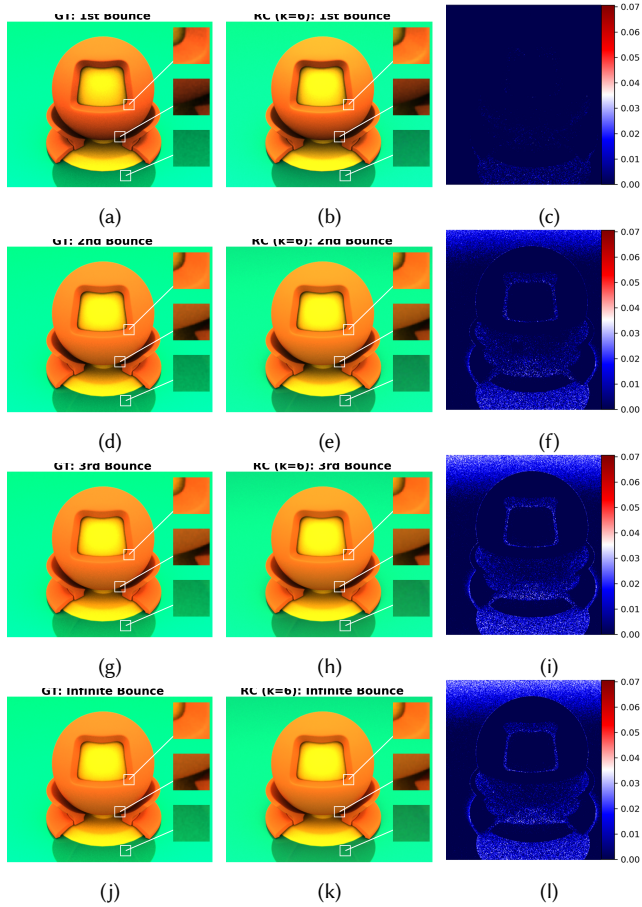


Fig. 8. Multi-bounce rendering results. Columns (left to right) show the ground-truth spectral rendering, our results with $k = 6$, and the per-pixel MSE map. Rows (top to bottom) correspond to 1, 2, and 3 bounces, and an “infinite-bounce” configuration implemented as unbounded path depth in Mitsuba v0.5 (*path* integrator, *maxDepth=-1*). The MSE increases slightly from 1 to 2 bounces, then remains approximately constant for 3 bounces and the infinite-depth setting, while the renderings remain perceptually similar.

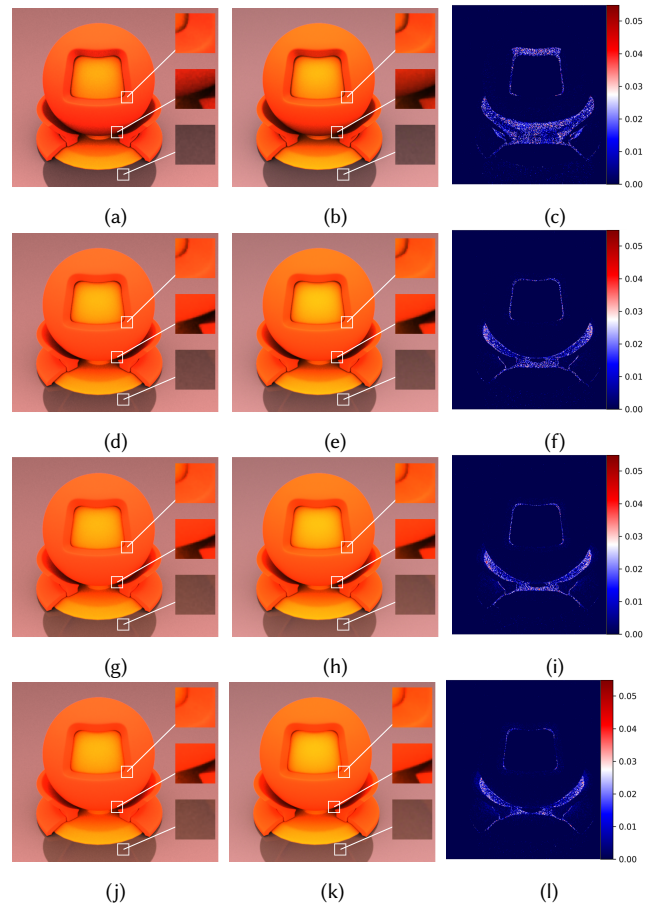


Fig. 9. Multi-bounce rendering test under *narrowband illumination*. Columns (left to right) show the ground-truth spectral rendering, our results with $k = 6$, and the per-pixel MSE map; rows (top to bottom) correspond to 1, 2, and 3 bounces, and an “infinite-bounce” configuration (Mitsuba v0.5 *path*, *maxDepth=-1*). In contrast to the broadband case, the MSE decreases slightly with increasing bounce count: $8.17 \times 10^{-4} \rightarrow 7.88 \times 10^{-4} \rightarrow 7.20 \times 10^{-4} \rightarrow 7.11 \times 10^{-4}$.